ARTICLE   OPEN

Check for updates

Quantum transport and localization in 1d and 2d tight-binding lattices

Amir H. Karamlou [1,2 ✉], Jochen Braumüller [1], Yariv Yanay [3], Agustin Di Paolo [1], Patrick M. Harrington[1], Bharath Kannan [1,2], David Kim[4], Morten Kjaergaard [1], Alexander Melville[4], Sarah Muschinske[1,2], Bethany M. Niedzielski [4], Antti Vepsäläinen [1], Roni Winik [1], Jonilyn L. Yoder[4], Mollie Schwartz [4], Charles Tahan[3], Terry P. Orlando[1,2], Simon Gustavsson [1] and William D. Oliver [1,2,4,5 ✉]

Particle transport and localization phenomena in condensed-matter systems can be modeled using a tight-binding lattice Hamiltonian. The ideal experimental emulation of such a model utilizes simultaneous, high-fidelity control and readout of each lattice site in a highly coherent quantum system. Here, we experimentally study quantum transport in one-dimensional and two-dimensional tight-binding lattices, emulated by a fully controllable 3×3 array of superconducting qubits. We probe the propagation of entanglement throughout the lattice and extract the degree of localization in the Anderson and Wannier-Stark regimes in the presence of site-tunable disorder strengths and gradients. Our results are in quantitative agreement with numerical simulations and match theoretical predictions based on the tight-binding model. The demonstrated level of experimental control and accuracy in extracting the system observables of interest will enable the exploration of larger, interacting lattices where numerical simulations become intractable.

INTRODUCTION

Single-particle dynamics and transport in periodic solids is well described by the tight-binding model[1]. This model is widely used to calculate the electronic band structure of condensed matter systems and to predict their transport properties, such as the conductance[2,3]. In the presence of a periodic lattice potential, the wavefunction of a given quantum particle overlaps neighboring lattice sites, leading to extended Bloch wavefunctions[1]. In the absence of lattice disorder, the particle propagation is ballistic and is described by a continuous-time quantum random walk[4]. This is in contrast to classical diffusive transport, where the propagation is quadratically slower in time[5].

The quantum nature of transport in lattices leads to the emergence of non-local correlations and entanglement between lattice sites. However, lattice inhomogeneity causes scattering and leads to quantum interference that tends to inhibit particle propagation, a signature of localization[6,7]. The wavefunction of a localized particle rapidly decays away from its initial position, effectively confining the particle to a small region of the lattice.

Here, we study Anderson localization and Wannier-Stark localization in one-dimensional (1d) and two-dimensional (2d) tight-binding lattices. In the presence of random disorder of the lattice site energies, a particle wavefunction becomes spatially localized, known as Anderson localization[6]. In the context of electrical transport, this phenomenon alters the transport properties, e.g., decreasing the conductance by increasing the degree of localization, ultimately leading to an insulating state. Alternatively, the particle can be localized in the presence of a potential gradient across the lattice, e.g., as created in the transport case by an external, static electric field, referred to as Wannier-Stark localization[7]. The potential gradient induces a position-dependent phase shift in the particle wavefunction and causes

the particle to undergo periodic Bloch oscillations in a confined region[8]. While the dynamics of these oscillations are challenging to observe in naturally occurring solid-state materials[9], they can be directly emulated and experimentally studied using engineered quantum systems.

Anderson localization has been experimentally realized in Bose-Einstein condensates[10,11], atomic Fermi gases[12], and photonic lattices[13,14]. Similarly, Bloch oscillations and Wannier-Stark localization have been observed in optical lattices[9,15], semiconductor superlattices[16], and photonic lattices[17,18]. However, these demonstrations were limited to varying degrees by a lack of control and simultaneous readout of each individual site. Therefore, these experiments could not fully explore the different localization regimes and spatial dimensions of the tight-binding model in a single experimental instantiation.

Superconducting quantum circuits are highly-controllable quantum systems that enable us to probe the properties of lattice models. By engineering the Hamiltonian of the superconducting quantum circuit, we can emulate the dynamics of the lattice Hamiltonian, and we can use single- and two-qubit gate operations for state preparation and tomographic state read-out[19–23]. Site-selective qubit control, strong qubit-qubit interactions, and long coherence times relative to typical gate times combined with the capability of simultaneously applying gates and performing tomographic state readout on all sites make this a promising platform for studying models of information propagation, many-body entanglement, and quantum transport.

In this work, we use a 9-qubit superconducting circuit to emulate the dynamics of single-particle quantum transport and localization in 1d and 2d tight-binding lattices. We probe the entanglement formed in the lattice as a result of the particle propagation. We then realize Anderson localization by
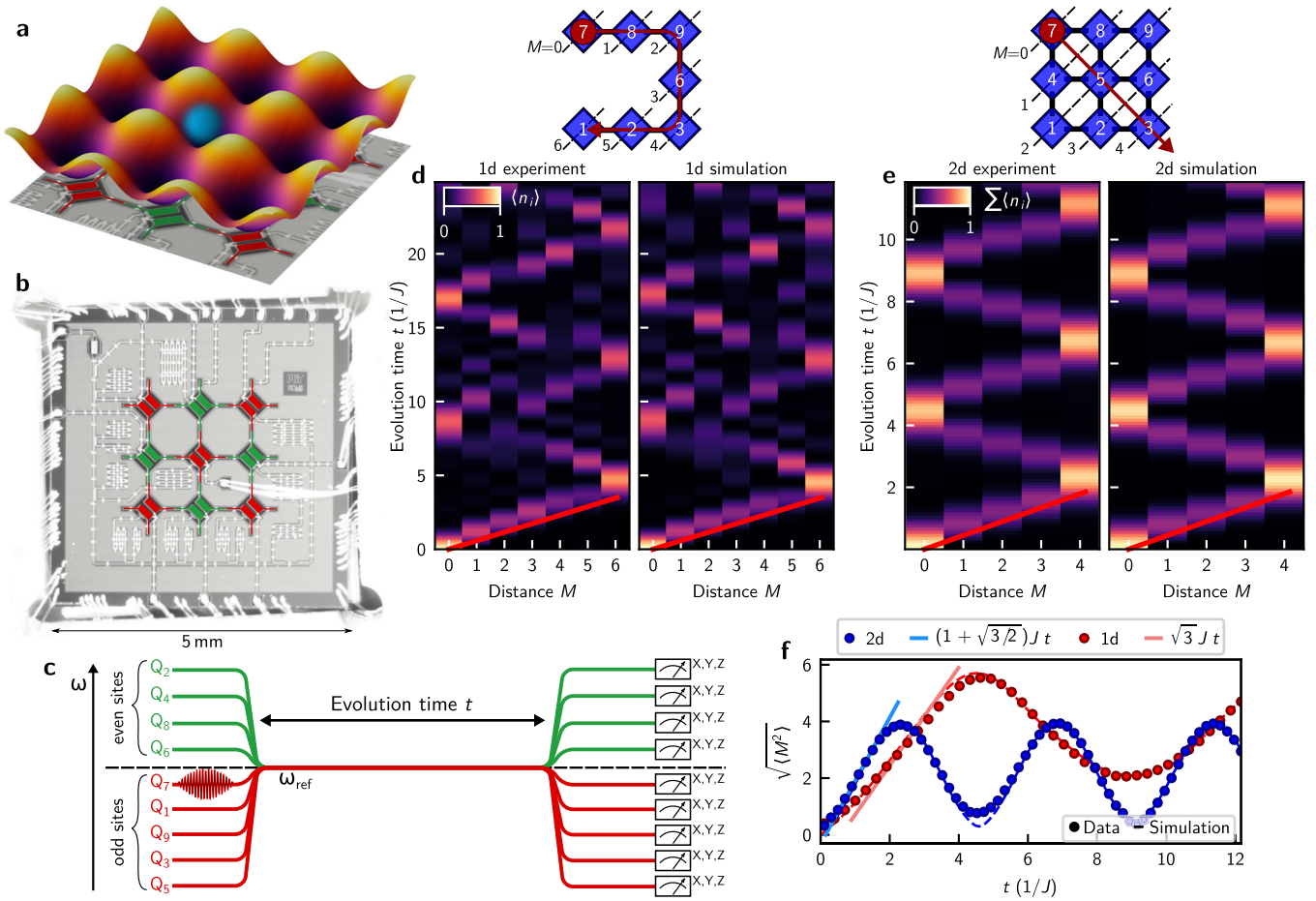
Fig. 1 Experimental concept and quantum random walks. a 2d periodic potential emulated by the superconducting quantum circuit. **b** Optical image of the 3×3 superconducting qubit lattice used in the experiment. The capacitor pads of the transmons qubits are false colored. **c** Operation sequence of the experiments. Each qubit is initially detuned from ω_{ref} and can be addressed individually, and simultaneously. They are brought on resonance to emulate evolution under $\hat{H}$ for time t. The system dynamics are frozen by once again detuning the qubits, and all nine qubits are measured simultaneously. **d** A 1d quantum random walk with a single excitation (particle) initialized at the edge of the lattice (site 7). **e** A 2d quantum random walk with a single excitation (particle) initialized at the corner of the lattice (site 7). **f** The spatial propagation of the particle is measured by the root of the second moment of position ($\sqrt{\langle M^2 \rangle}$) in the 1d and 2d lattices. The excitation initialized at the edge of the 1d chain exhibits ballistic propagation in time and with propagation speed $v_g = \sqrt{3}J$ (red line), whereas an excitation initialized in the corner of a 2d lattice exhibits an increased propagation speed $v_g = (1 + \sqrt{3/2})J$ (blue line).

implementing random disorder of the on-site energies with tunable strength, and extract the dependence of the propagation mean free path on the disorder strength in a regime with no analytical solution. Additionally, we study Wannier-Stark localization in the presence of isotropic and anisotropic potential gradients, and find close agreement between our experiments and theoretical predictions.

The close agreement between our experimental results, simulations, and theoretical predictions results from high-fidelity, simultaneous qubit control and readout, an accurate calibration, and an accounting for the relevant decoherence mechanisms in this system. Although our experiments are performed on a small lattice that can still be simulated on a classical computer, they demonstrate a platform for exploring larger, interacting systems where numerical simulations become intractable.

RESULTS

Experimental setup

Our device consists of a 3×3 array of capacitively coupled superconducting transmon qubits[24] (Fig. 1b), where qubit excitations correspond to particles in the lattice model. In the

single-particle regime, the effective system Hamiltonian in the rotating frame with reference frequency ω_{ref} is described by the tight-binding Hamiltonian:

$$\hat{H}/\hbar = -\sum_{\langle i,j \rangle} J_{i,j} \hat{\sigma}_i^\dagger \hat{\sigma}_j + \sum_i \epsilon_i \hat{\sigma}_i^\dagger \hat{\sigma}_i \tag{1}$$

where $\hat{\sigma}_i^\dagger$ ($\hat{\sigma}_i$) are the two-level creation (annihilation) operators for each lattice site i. The first term in the Hamiltonian represents particle tunneling between neighboring sites with rate $J_{i,j}$, realized here with an average strength of $J/2\pi = 8.1$ MHz at $\omega_{\mathrm{ref}} = 5.5$ GHz. The second term represents the particle occupation energy of sites i with the corresponding site energies $\epsilon_i = \omega_i - \omega_{\mathrm{ref}}$, where ω_i is the fundamental transition frequency of the transmon at site i. By using flux-tunable transmons, the energy of each site can be individually set over the range $3.0 \text{ GHz} \lesssim \omega_i/2\pi \lesssim 5.5 \text{ GHz}$. This tunability enables us to realize arbitrary energy landscapes and to isolate sub-lattices (e.g., one-dimensional chains) by detuning certain qubits from their neighbors so that they do not interact with the rest of the lattice. The transmons have an average anharmonicity of $U/2\pi = -244$ MHz, which corresponds to the on-site interaction energy of two particles occupying the same site. The system operates in the $J \ll |U|$ limit such that

each lattice site can be occupied by at most a single particle, generally realizing the hard-core Bose-Hubbard model[25,26].

Our experiments feature simultaneous, site-resolved, single-shot dispersive qubit readout with an average qubit state assignment fidelity of 95%. In addition, we are able to control the energy of each site with an average precision $\langle \Delta \epsilon \rangle < (2\pi)$ 200 kHz ($\approx J/40$). These features are crucial to accurately emulate the 1d and 2d tight-binding model with different lattice potential configurations, and allow us to achieve close agreement between numerical simulations and experiment.

Quantum random walk

Quantum random walks (QRWs) are the quantum mechanical analog of classical random walks. The spatial propagation of the particle throughout the lattice, relative to its initial location, is quantified by the mean square displacement $\langle M^2 \rangle = \sum_i p_i M_i^2$, where p_i is the probability of finding the particle on site i, and M_i is the Manhattan (1-norm) distance between site i and the initialization site. Quantum properties such as single-particle superposition and interference result in a qualitative difference between classical and quantum random walks: a classical random walk propagates diffusively in time with $\sqrt{\langle M^2 \rangle} \propto \sqrt{t}$, whereas a QRW exhibits ballistic propagation with a mean-square displacement $\sqrt{\langle M^2 \rangle} \propto t$[27].

In order to experimentally observe particle propagation through QRWs, we first implement a tight-binding lattice with uniform site energies ($\epsilon_i = 0$). We compare the respective propagation speeds for QRWs in a seven-site 1d chain (Fig. 1d) and a 2d 3×3 lattice (Fig. 1e). We inject a particle at the end (corner) of the 1d (2d) lattice and observe its propagation by tracking the excitation numbers $\langle \hat{n}_i \rangle = \langle \hat{\sigma}_i^\dagger \hat{\sigma}_i \rangle$ on each lattice site versus evolution time t.

In the 1d case, the particle traverses the lattice and eventually reflects off the opposite end of the chain[28]. All intermediate sites are coupled to their two nearest neighbors, with the end sites being coupled to only one. Hence, the QRW propagates in both directions: an excitation is reemitted in both the forward and reverse directions (interim sites), or the direction is reversed (end sites). Quantum interference between these multiple trajectories alters the particle wavepacket as it evolves in time. The resulting QRW pattern for a seven-site chain features a non-trivial evolution that agrees well with numerical simulation (Fig. 1d).

In the 2d QRW, the particle propagates along its diagonal symmetry axis, analogous to a QRW on a binary tree[5]. Here, the particle position is defined by the sum of the site populations at a given Manhattan distance M from the injection site. The quantum interference leading to the simple back-and-forth pattern as a result of reflection is exceptional and arises from the high-degree of symmetry present in a 3×3 lattice (Fig. 1e). Such a high-degree of symmetry is similarly observed in 1d for a five-site chain (see Supplementary Material).

To verify these experimental results, we perform Lindblad master equation simulations (see Supplementary Material) based on the Hamiltonian in Eq. (1). We find excellent agreement between experimental data and numerical simulations by using the measured coupling strengths J_{ij} between neighboring lattice sites i, j, and taking into account qubit relaxation and decoherence.

Both 1d and 2d QRWs exhibit ballistic propagation, and the propagation speed in 2d is faster than in 1d due to the constructive interference between multiple propagation paths leading to each site in 2d (Fig. 1f). The average group velocity v_g of transport depends on the dimensionality of the lattice and the starting position of the particle with respect to the lattice boundaries. For a 1d QRW, a particle prepared at one end of the lattice initially propagates with $v_g = J$, because it interacts with only one other lattice site. At later times, prior to reflection from

the other end, it reaches a steady state value of $v_g = \sqrt{3}J$, in agreement with theory for infinitely long chains[27]. In contrast, we observe that a particle prepared in the corner of a 3×3 lattice propagates with an initial group velocity $v_g = \sqrt{2}J$ (due to the coupling to its two nearest neighbors) and a steady state average velocity of $v_g = (1 + \sqrt{3/2})J$ (see Supplementary Material). During the QRW, certain sites become entangled as the particle propagates through the lattice, a phenomenon that underpins its intrinsic quantum character[28,29]. We observe the emergence of entanglement as a result of the system time evolution via non-local spatial correlations. We quantify the entanglement formed among the qubits at the same distance from the particle initialization site, and study how the QRW entangles this site with the rest of the lattice in a coherent manner. The amount of entanglement within a two-qubit sub-system, described by $\rho_{i,j}$, can be quantified using the pairwise concurrence[30]:

$$\mathcal{C}_{i,j} \equiv \mathcal{C}(\rho_{i,j}) = \max\{0, \lambda_1 - \lambda_2 - \lambda_3 - \lambda_4\} \quad (2)$$

where $\{\lambda_\mu\}$ (in decreasing order) are the eigenvalues of the Hermitian matrix $R \equiv \sqrt{\sqrt{\rho_{i,j}}\tilde{\rho}_{i,j}\sqrt{\rho_{i,j}}}$. Here, $\tilde{\rho} = (\sigma_y \otimes \sigma_y)\rho^*(\sigma_y \otimes \sigma_y)$ is the spin-flipped density matrix obtained through complex conjugation and applying Pauli-Y operators (σ_y) to each qubit. Concurrence is a monotone entanglement metric for two-qubit states that takes values between zero (product state) and one (maximally entangled). To reconstruct the two-qubit density matrix $\rho_{i,j}(t)$ and calculate the pairwise concurrence $\mathcal{C}_{i,j}(t)$, we perform two-qubit state tomography for various evolution times t of the QRW.

We measure the concurrence formed during a 2d QRW between site pairs at the same Manhattan distance from the particle initialization site (Fig. 2a). Lattice sites at the same Manhattan distance become partially entangled as the particle traverses them, as indicated by an increase in the concurrence. This approach faithfully describes the quantum correlations in the sub-systems comprising of two sites $M = 1, 3$. However, the sub-system of sites at $M = 2$ contains three qubits, and solely considering pairwise concurrence values does not fully capture the entanglement within this sub-system.

Using the pairwise concurrence values between the sites at $M = 2$, we calculate the lower-bound of the distributed concurrence $\mathcal{C}_{i(j,k)}^{\min}$ for each site in this sub-system (Fig. 2b). For a state consisting of three qubits (i, j, k), the concurrence $\mathcal{C}_{i(j,k)}$ between site i and the system comprised of the two remaining sites (j, k) can be lower-bounded using the pairwise concurrences[31]:

$$\mathcal{C}_{i(j,k)}^2 \geq \mathcal{C}_{i,j}^2 + \mathcal{C}_{i,k}^2. \quad (3)$$

Using the extracted pairwise and distributed concurrence values, we compute the average of the lower-bound concurrence $\overline{\mathcal{C}}$ for sub-systems consisting of qubits that are at the same distance from the initial particle position (Fig. 2c). $\overline{\mathcal{C}}$ is equal to the pairwise concurrence for sub-systems containing two qubits ($M = 1, 3$), and an average of $\mathcal{C}_{i(j,k)}^{\min}$ for the sub-system containing three qubits ($M = 2$). The emergence of entanglement reflects the particle trajectory during the QRW (see Supplemental Material) and is in agreement with the light-cone of the measured quantum information propagation using out-of-time-ordered correlators[26] within the Lieb-Robinson bounds[32] (see Supplementary Material).

While the initially prepared single-particle state is separable from the rest of the lattice, the QRW, mediated by the nearest-neighbor interactions, creates and distributes entanglement to varying degrees throughout the lattice. For a system containing exactly a single particle, Eq. (3) becomes an equality and can be generalized to a system with more than three sites[31]. In our 3×3 lattice, the concurrence between the initialization site (site 7) and the rest of the system $\mathcal{C}_{7,\text{lattice}}$ can be extracted exactly using
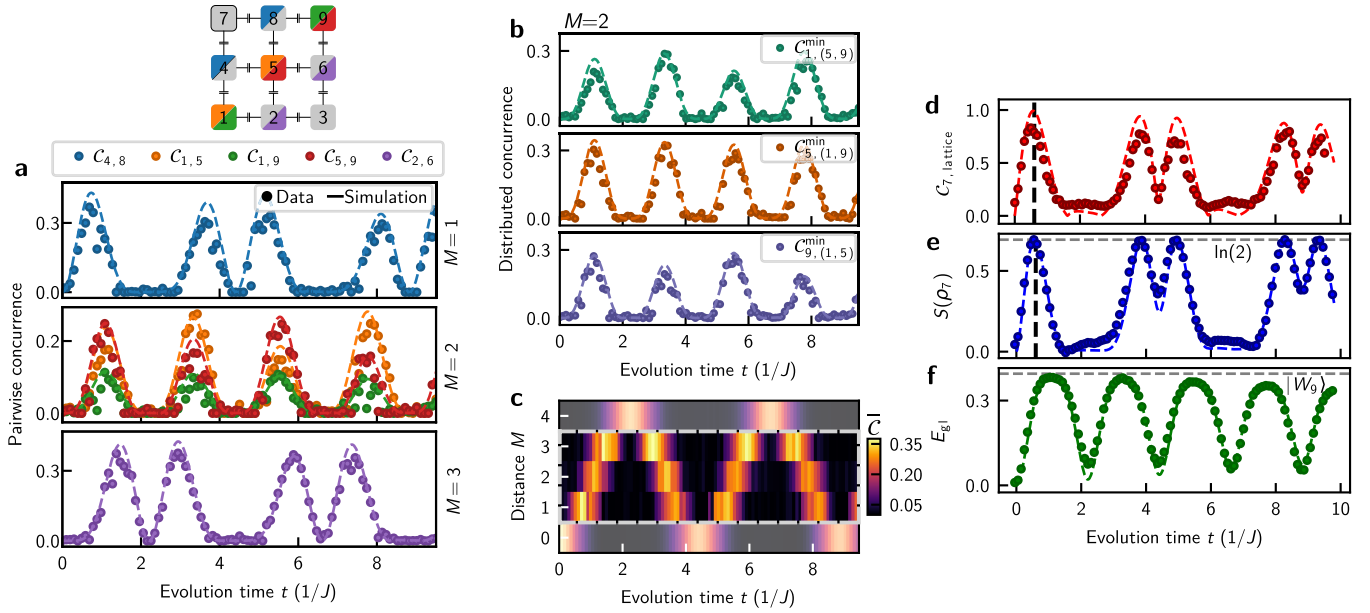
Fig. 2 Entanglement propagation in 2d lattice. a Evolution of the concurrence between pairs of sites at the same distance from the propagation source. **b** Distributed concurrence formed among the three qubits at distance $M = 2$ from the particle initialization site. $\mathcal{C}^{\min}_{i,(j,k)}$ represents the minimum concurrence between qubit i and the sub-system consisting of qubits j and k. **c** Average minimum concurrence formed between the sites along the diagonal symmetry axis of the lattice. We display the population on the sites at distance 0 and 4 as a reference (shaded regions). **d** Concurrence of the propagation source and the rest of the lattice. The source becomes maximally entangled with the remaining of the lattice at $t \simeq (2J)^{-1}$. **e** The von Neumann entropy of the propagation source (site 7), reaching a maximum value of (2) at time $t \simeq (2J)^{-1}$. **f** Global entanglement E_{gl} among the lattice sites. The upper-bound of E_{gl} for a single-particle tight-binding model is set by the global entanglement of the 9-qubit W-state $|W_9\rangle$.

pairwise concurrence values (see Supplementary Material):

$$\mathcal{C}^2_{7,\text{lattice}} = \sum_{j' \neq 7} \mathcal{C}^2_{7,j'}. \tag{4}$$

We observe that the quantum state of the initialization site becomes fully entangled with the larger system at time $t \simeq (2J)^{-1}$ (Fig. 2d). The coherent propagation leads to the fall and revival of the concurrence as the particle wavefunction evolves with time, with $\mathcal{C}_{7,\text{lattice}} = 0$ when site 7 is in a pure ground or excited state. This behavior is in agreement with the evolution of the von Neumann entropy $S(\rho_7) = -\text{tr}(\rho_7 \ln \rho_7)$ (Fig. 2e), where ρ_7 is the single-qubit density matrix of site 7. The von Neumann entropy is a measure for the entanglement of the lattice site with its environment, and takes a value of $\ln(2)$ for a maximally entangled state. The dynamical revival of both $\mathcal{C}_{7,\text{lattice}}$ and $S(\rho_7)$ indicates that site 7 becomes predominantly entangled with the rest of the lattice, rather than with the uncontrolled environmental degrees of freedom related to decoherence.

Time evolution under an interacting Hamiltonian creates entanglement among the nine sites in our system. We quantified the entanglement between different sub-systems of the lattice using concurrence and von Neumann entropy, however, the overall entanglement formed in the lattice is also of interest for studying the quantum properties of the system. Without the need for full quantum state tomography, we probe the global entanglement E_{gl} in the many-body system, beyond the non-local correlations formed between sub-systems, by extracting the average purity of all N sites[33,34]

$$E_{gl} = 2 - \frac{2}{N} \sum_{j=1}^{N} \text{tr}(\rho_j^2), \tag{5}$$

where ρ_j is the reduced density matrix describing site j. In Fig. 2f, we observe that the global entanglement reaches a maximum value when the particle is not concentrated on either corner of the lattice, but rather extends across all lattice sites. In our 2d lattice,

E_{gl} is upper-bounded by the global entanglement in the 9-qubit W-state $|W_9\rangle$[35], where $|W_N\rangle = \frac{1}{\sqrt{N}} \sum_\pi |\pi(0...01)\rangle$ is the superposition of all single-particle state permutations. At later times, the maximum global entanglement in the system decreases as a result of system decoherence. Using this metric, we study the degree of entanglement in the lattice as a result of the particle evolution.

Anderson localization

We have so far explored quantum transport in lattices with uniform site energies. However, particle propagation is significantly impacted by the introduction of random disorder in the site energies, leading to Anderson localization[6]. In the presence of disorder in 1d and 2d lattices, the particle wavefunction becomes spatially localized, regardless of the disorder strength in the thermodynamic limit[36]. In our experiments, we emulate the Anderson localization regime by introducing disorder with strength δ, where site energies are randomly sampled from a uniform distribution $\epsilon_i \in [-\delta/2, \delta/2]$. As a result, wavefunction scattering causes the particle to lose phase coherence on the length scale of the mean-free path l. While an analytical form for the mean free path can be derived in the limit of weak ($\delta \ll J$) and strong ($\delta \gg J$) disorder[37,38], there are no known analytical expressions in the intermediate disorder regime[39].

We examine the degree of localization by measuring the increase in average population $\overline{\langle n_s \rangle}$ of the initially prepared lattice site and the decrease in particle spread $\sqrt{\langle M^2 \rangle}$ for increasing disorder strengths δ, each averaged over 50 random lattice realizations. As the disorder strength increases, a higher steady-state population remains on the source site as a result of the tight-binding interaction (Fig. 3a, c), while the average particle spread away from the source decreases (Fig. 3b, d) for both 1d and 2d lattices. For a given disorder strength, the particle is more confined in a 1d lattice compared to a 2d lattice; in 2d, the probability of transport is relatively greater in the presence of
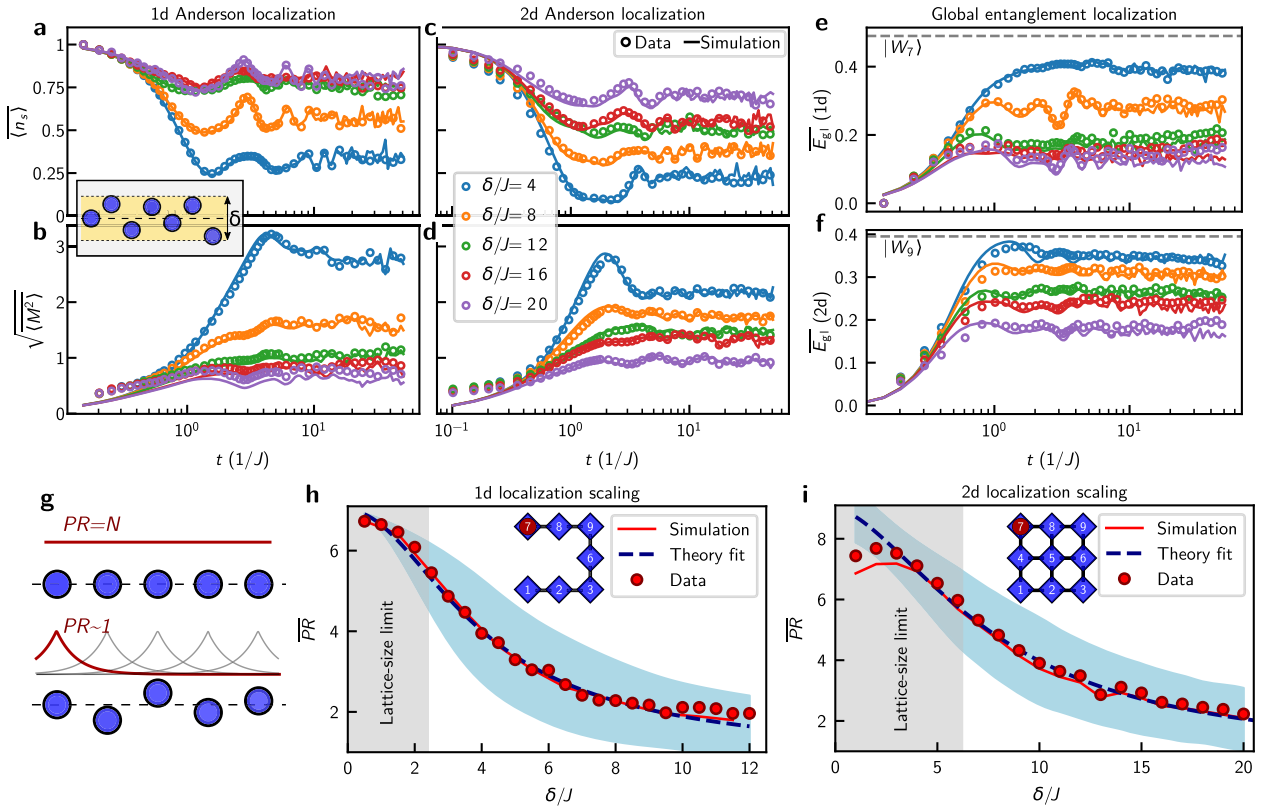
Fig. 3 Anderson localization. Population at the propagation source (**a**) and particle root mean-squared distance from the source (**b**) for different 1d lattice disorders. Each point is averaged over 50 disorder realizations. Population at the propagation source (**c**) and particle mean-squared distance from the source (**d**) for different 2d lattice disorders. Each point is averaged over 50 disorder realizations. The global entanglement among the sites in the 1d lattice (**e**) and 2d lattice (**f**) measured at different disorder strengths averaged over 50 realizations. **g** The wavefunction for a completely delocalized state takes the value of PR = N, whereas PR = 1 for a wavefunction fully localized to a single site. **h** 1d Anderson localization participation ratio $\overline{PR}$ scaling with disorder strength, obtained using 60 random lattice realizations for each value of disorder strength δ. The blue shaded region indicates the simulated statistical uncertainty interval (±1 standard deviation) as a result of lattice randomization. **i** 2d Anderson localization $\overline{PR}$ scaling with disorder strength, obtained using 180 random lattice realization for each value of δ.

disorder as propagation occurs along multiple paths between two sites. As a result of localization caused by disorder, the emergence of multipartite entanglement in the tight-binding lattice is inhibited: in Fig. 3e, f, we report a decrease in the steady state value for the average global entanglement of the system, $\overline{E_{gl}}$, with increasing disorder strength, due to spatial localization of the particle wavefunction. With one excitation, the confinement effects for seven-site chain causes a relatively greater deviation from the maximum value (E_{gl} of $|W_7\rangle$) compared to the 2d lattice.

We quantify the localization of the wavefunction in a lattice with N sites using the participation ratio PR, defined as[40]

$$PR(\psi) = \left(\sum_i^N |\psi_i|^4\right)^{-1} = \left(\sum_i^N |n_i|^2\right)^{-1}. \quad (6)$$

If the particle wavefunction is completely delocalized, then PR = N, whereas PR = 1 for a wavefunction fully localized to a single site (Fig. 3g). In our experiments, PR for each lattice realization is calculated using the time-averaged population on each site after the tight-binding model dynamics reach steady state[40]. In order to reduce the impact of qubit relaxation on these measurements, we use the averaged site populations between 100 ns and 400 ns ($5/J \lesssim t \lesssim 20/J$) to calculate PR (see Supplementary Material for an example). We experimentally extract the participation ratio $\overline{PR}$ averaged over different random lattice realizations, at different disorder strengths for both a 1d and 2d lattice. As δ increases, the particle wavefunction becomes more spatially confined and

$\overline{PR}$ decreases. For weak disorder strengths, we find the localization length to be larger than the lattice size (gray region in Fig. 3h, i), imposing a limitation on our experiments caused by boundary effects.

In a finite 1d lattice, the participation ratio is related to the localization length ξ_{1d} through the expression $PR(\xi_{1d}) = \coth(1/\xi_{1d})\tanh(N/\xi_{1d})$ (see Supplementary Material). The 1d localization length ξ_{1d} scales directly with the mean free path l as $\xi_{1d} = l$[36]. We experimentally extract the dependence of the mean free path on the disorder strength, taking the form $l = a(J/\delta)^\gamma$, in our seven-site chain by realizing 60 random lattice disorders for different disorder strengths and calculating $\overline{PR}$ (Fig. 3h). In the 1d case, we find $\gamma = 1.0 \pm 0.03$ and $a = 17.0 \pm 1.05$ (in units of the lattice spacing) through fitting.

In a 2d $n \times n$ lattice, the participation ratio is related to the localization length through the expression $PR(\xi_{2d}) = \coth^2(1/\xi_{2d})\tanh^2(n/\xi_{2d})$ (see Supplementary Material), where the localization length takes the form $\xi_{2d} = l \, e^{\frac{\pi}{2}kl}$ with a lattice-dependent factor k[36]. For weak disorder, the 2d $\overline{PR}$ scales exponentially with the mean free path. Consequently, the scaling for small values of δ is difficult to observe in our small lattice, and hence the value of k cannot be obtained with high accuracy. We extract the 2d $\overline{PR}$ in our 3×3 lattice (Fig. 3i) over 180 random lattice realizations for different disorder strengths, and for large values of δ we find the parameters for the mean free path $\gamma = 0.80 \pm 0.02$ and $a = 12.98 \pm 0.60$ (in units of the lattice spacing). In a 2d lattice, we notice that the extracted mean free path exhibits a
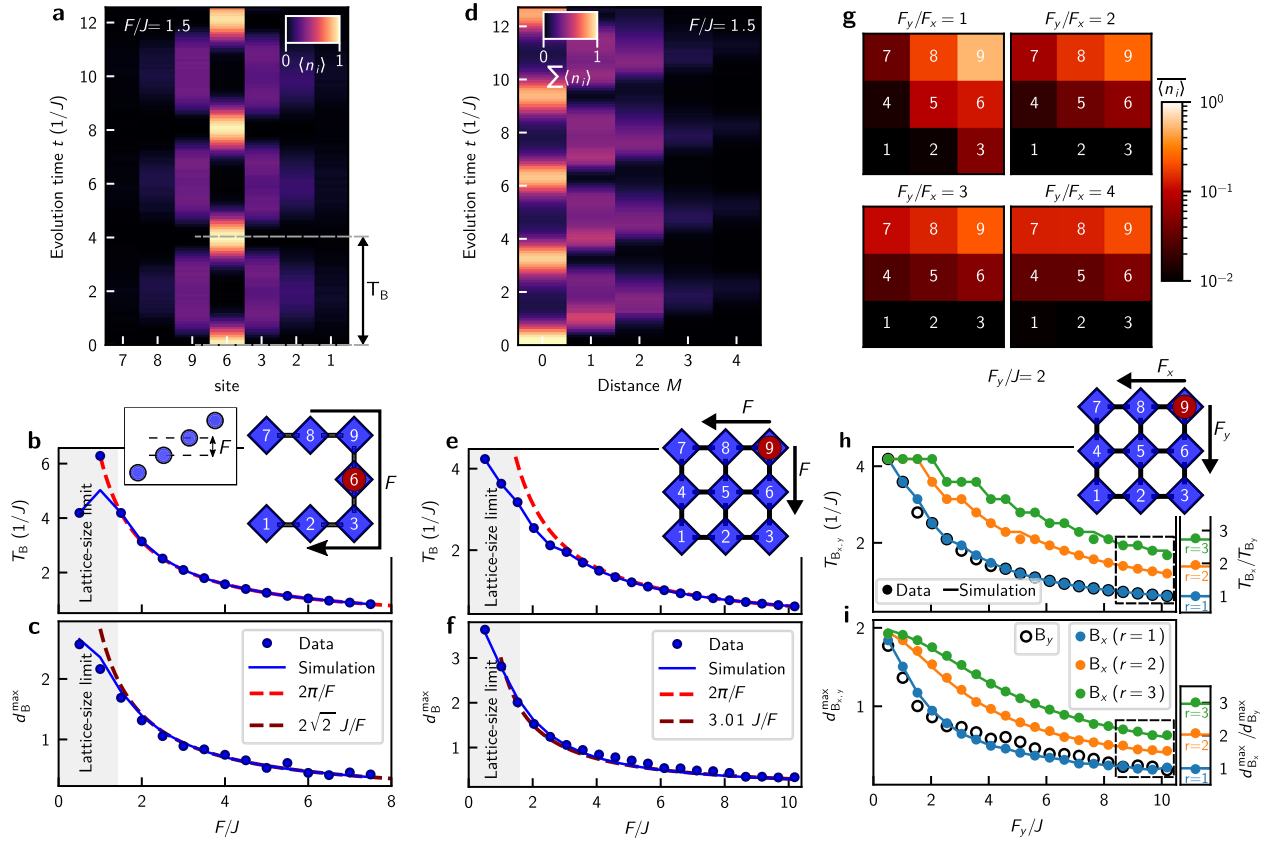
Fig. 4 Wannier-Stark localization. a Exemplary 1d Bloch oscillation with a particle initialized at the center of the lattice. The particle undergoes a spatially periodic breathing motion before re-converging at the initialization site. **b, c** 1d Bloch oscillation period T_B and maximum particle spread d_B^{max} scaling with the potential gradient strength F. **d** Exemplary 2d Bloch oscillation with an isotropic potential gradient with a particle initialized at the corner of the lattice. The particle undergoes periodic Bloch oscillations along the diagonal symmetry axis of the lattice. **e, f** Isotropic 2d Bloch oscillation period T_B and maximum particle spread d_B^{max} depending on F. **g** Time-averaged population $\overline{\langle n_i \rangle}$ on each site for different anisotropy ratio $r = F_y/F_x$. As r increases, the propagation gets skewed towards the horizontal axis. **h, i** T_B and d_B^{max} along the horizontal (B_x) and vertical (B_y) direction of the lattice of anisotropic fields at different values of r. Inset on the right side of the figure show the values of T_{B_x}/T_{B_y} and $d_{B_x}^{max}/d_{B_y}^{max}$ obtained from our experiments and numerical simulations highlighted using a dashed box.

weaker dependence on the disorder strength, consistent with our earlier observations.

Wannier-Stark localization

A particle in the tight-binding lattice is localized also in the presence of a static electric field, which creates a potential gradient across lattice site energies[7]. We emulate the effect of an electric field by creating a gradient in the lattice site energies ϵ_i. The resulting potential gradient causes the particle to become spatially confined due to the emergence of a band-gap in the lattice band structure[9]. This phenomenon is referred to as Wannier-Stark localization[7,15,41]. The effective field creates a linear gradient $\vec{F}$ along the lattice axis, where $\vec{F} = \nabla \epsilon_i$, and causes the particle to undergo periodic Bloch oscillations.

We demonstrate Bloch oscillations in a 1d chain for the field strength $F/J = 1.5$ ($F = |\vec{F}|$) observing a spatially periodic breathing motion with a probability up to 99% of the particle reviving at the initialization site (Fig. 4a). By repeating the experiment for different values of F, we observe that a particle initialized in the center of the lattice oscillates with a Bloch period $T_B = 2\pi/F$ (Fig. 4b) and a maximum particle spread of $d_B^{max} = \max(\sqrt{\langle M^2 \rangle}) = 2\sqrt{2}J/F$ (Fig. 4c) from the initialization site, in agreement with theory[8]. The finite lattice size causes the boundaries to have a notable effect on the oscillation for small values of F (gray region of Fig. 4b, c), namely the decrease in the

oscillation period and limiting the particle spread. We observe a similar periodic motion along the diagonal symmetry axis of the lattice in 2d (Fig. 4d) for an isotropic field ($F = F_x = F_y$). The Bloch period of a particle initialized in the corner of a 2d lattice with this symmetric gradient exhibits the same scaling with F as in 1d. We find that the maximum particle spread in a 2d lattice scales as $d_B^{max} = \max(\sqrt{\langle M^2 \rangle}) = 3.01 \pm 0.01 J/F$, where we obtained the value 3.01 from a data fitting procedure. Wannier-Stark localization is less pronounced in 2d compared to 1d for the same potential gradient, similar to the trend we observe in the Anderson localization regime and in agreement with theoretical predictions[42].

We also explore the effect of non-isotropic fields in a 2d lattice by independently controlling the potential gradients along the horizontal (F_x) and the vertical (F_y) axes, respectively. In Fig. 4g, we show the time-averaged population of each site during the first 500 ns ($\approx 25/J$) of evolution as a result of different field ratios $r = F_y/F_x$. In the presence of the same field along both lattice axes ($r = 1$), the particle is localized along the diagonal symmetry axis of the lattice (Fig. 4g top left). As r increases by decreasing F_x while keeping F_y fixed, the particle becomes less localized along the F_x-direction, skewing the propagation direction.

In the absence of boundary effects, the relation between Bloch oscillation periods T_{B_x} and T_{B_y} along each lattice axis depends on the net field direction, namely $T_{B_x} = r T_{B_y}$ (Fig. 4h). For rational values of r, the total 2d Bloch period T_B is the least

common multiple of the one-dimensional Bloch periods along each axis[42]. A similar relationship holds for the maximum particle spread in each direction: $d_{B_x}^{max} = r\, d_{B_y}^{max}$ (Fig. 4i). In our experiments, we investigate these relations by measuring T_{B_x} (see Fig. 4h) and $d_{B_x}^{max}$ (see Fig. 4i) for $r = 1, 2, 3$ (solid circles) while varying F_y. The data match simulation (solid lines) of the 3×3 system very well. We additionally measured T_{B_y} and $d_{B_y}^{max}$, which are nominally unchanged for $r = 1, 2, 3$, and present the values measured for isotropic potential gradients (open circles). This enables us to obtain experimental estimates for r by taking the ratio between the experimentally measured Bloch periods T_{B_x}/T_{B_y} (Fig. 4h, right panel) and the maximum spread $d_{B_x}^{max}/d_{B_y}^{max}$ (Fig. 4i, right panel). The ratios for each r are estimated from highlighted points in Fig. 4h, i.

DISCUSSION

In this work, we have emulated quantum particle propagation and localization in 1d and 2d tight-binding lattices using a 3×3 array of superconducting qubits. We have measured the coherent dynamics of different entanglement metrics, such as concurrence and the von Neumann entropy, during quantum transport using simultaneous control and readout. We have further investigated localization in different regimes of the tight-binding model, with random disorder resulting in Anderson localization and with a potential gradient causing Wannier-Stark localization and Bloch oscillations. We have studied Anderson localization in a disorder regime that lacks an analytical form, and used our data to extract the dependence of the propagation mean free path in finite 1d and 2d lattices on the disorder strength. We have measured the degree of Wannier-Stark localization as a result of different potential gradients for both isotropic and anisotropic potentials, and have observed quantitative agreement in the properties of Bloch oscillations with theoretical predictions.

We can control all of the on-site energies with high precision compared to the coupling rate between neighboring sites. Furthermore, we can manipulate the lattice (qubit) energy landscape on timescales much shorter than the particle exchange (qubit-qubit interaction) and system coherence times by two orders of magnitude. This ability to accurately initialize and manipulate our system Hamiltonian combined with high-fidelity tomographic readout enables us to study tight-binding lattices under various configurations. For superconducting qubits, models based on calibrated qubit parameters and decoherence[43,44] have been demonstrated to accurately predict the behavior of multi-qubit processors[45,46]. These features form the basis for agreement between our experimental results and our simulations. The demonstrated degree of control in realizing different regimes of the tight-binding model in 1d and 2d serves as a blueprint for exploring larger and strongly interacting quantum lattices in the few-body[47] and the many-body localization regimes[40,48,49] or that contain a time-dependent Hamiltonian leading to interesting phenomena such as quantum scars[50] topological order[51] and the breakdown of the Magnus expansion[52].

DATA AVAILABILITY

The raw data used for generating the plots in this paper are available upon request.

REFERENCES

1. Slater, J. C. & Koster, G. F. Simplified LCAO method for the periodic potential problem. *Phys. Rev.* **94**, 1498–1524 (1954).
2. Goringe, C. M., Bowler, D. R. & Hernández, E. Tight-binding modelling of materials. *Rep. Prog. Phys.* **60**, 1447–1512 (1997).
3. Cleri, F. & Rosato, V. Tight-binding potentials for transition metals and alloys. *Phys. Rev. Lett.* **48**, 22–33 (1993).
4. Kempe, J. Quantum random walks: an introductory overview. *Contemp. Phys.* **44**, 307–327 (2003).
5. Childs, A. M., Farhi, E. & Gutmann, S. An example of the difference between quantum and classical random walks. *Quantum Inform. Process.* **1**, 35–43 (2002).
6. Anderson, P. W. Absence of diffusion in certain random lattices. *Phys. Rev.* **109**, 1492–1505 (1958).
7. Emin, D. & Hart, C. F. Existence of Wannier-Stark localization. *Phys. Rev. Lett.* **36**, 7353–7359 (1987).
8. Hartmann, T., Keck, F., Korsch, H. J. & Mossmann, S. Dynamics of Bloch oscillations. *N. J. Phys.* **6**, 2 (2004).
9. Ben Dahan, M., Peik, E., Reichel, J., Castin, Y. & Salomon, C. Bloch oscillations of atoms in an optical potential. *Phys. Rev. Lett.* **76**, 4508–4511 (1996).
10. Billy, J. et al. Direct observation of Anderson localization of matter waves in a controlled disorder. *Nature* **453**, 891–894 (2008).
11. Roati, G. et al. Anderson localization of a non-interacting Bose-Einstein condensate. *Nature* **453**, 895–898 (2008).
12. Kondov, S. S., McGehee, W. R., Zirbel, J. J. & DeMarco, B. Three-dimensional Anderson localization of ultracold matter. *Science* **334**, 66–68 (2011).
13. Lahini, Y. et al. Anderson localization and nonlinearity in one-dimensional disordered photonic lattices. *Phys. Rev. Lett.* **100**, 013906 (2008).
14. Schwartz, T., Bartal, G., Fishman, S. & Segev, M. Transport and Anderson localization in disordered two-dimensional photonic lattices. *Nature* **446**, 52–55 (2007).
15. Preiss, P. M. et al. Strongly correlated quantum walks in optical lattices. *Science* **347**, 1229–1233 (2015).
16. Feldmann, J. et al. Optical investigation of Bloch oscillations in a semiconductor superlattice. *Phys. Rev. Lett.* **46**, 7252–7255 (1992).
17. Morandotti, R., Peschel, U., Aitchison, J. S., Eisenberg, H. S. & Silberberg, Y. Experimental observation of linear and nonlinear optical bloch oscillations. *Phys. Rev. Lett.* **83**, 4756–4759 (1999).
18. Trompeter, H. et al. Bloch oscillations and Zener tunneling in two-dimensional photonic lattices. *Phys. Rev. Lett.* **96**, 053903 (2006).
19. Roushan, P. et al. Spectroscopic signatures of localization with interacting photons in superconducting qubits. *Science* **358**, 1175–1179 (2017).
20. Neill, C. et al. A blueprint for demonstrating quantum supremacy with superconducting qubits. *Science* **360**, 195–199 (2018).
21. Chiaro, B. et al. Direct measurement of non-local interactions in the many-body localized phase. http://arxiv.org/abs/1910.06024 (2019).
22. Ma, R. et al. A dissipatively stabilized Mott insulator of photons. *Nature* **566**, 51–57 (2019).
23. Gong, M. et al. Quantum walks on a programmable two-dimensional 62-qubit superconducting processor. *Science* **372**, 948–952 (2021).
24. Koch, J. et al. Charge-insensitive qubit design derived from the Cooper pair box. *Phys. Rev. A* **76**, 042319 (2007).
25. Yanay, Y., Braumüller, J., Gustavsson, S., Oliver, W. D. & Tahan, C. Two-dimensional hard-core Bose–Hubbard model with superconducting qubits. *npj Quantum Inf.* **6**, 58 (2020).
26. Braumüller, J. et al. Probing quantum information propagation with out-of-time-ordered correlators. *Nat. Phys.* **18**, 172–178 (2022).
27. Hoyer, S., Sarovar, M. & Whaley, K. B. Limits of quantum speedup in photosynthetic light harvesting. *New J. Phys.* **12**, 065041 (2010).
28. Yan, Z. et al. Strongly correlated quantum walks with a 12-qubit superconducting processor. *Science* **364**, 753–756 (2019).
29. Cheneau, M. et al. Light-cone-like spreading of correlations in a quantum many-body system. *Nature* **481**, 484–487 (2012).
30. Wootters, W. K. Entanglement of formation of an arbitrary state of two qubits. *Phys. Rev. Lett.* **80**, 2245–2248 (1998).
31. Coffman, V., Kundu, J. & Wootters, W. K. Distributed entanglement. *Phys. Rev. A* **61**, 5 (2000).
32. Lieb, E. H. & Robinson, D. W. The finite group velocity of quantum spin systems. *Commun. Math. Phys.* **28**, 251–257 (1972).
33. Meyer, D. A. & Wallach, N. R. Global entanglement in multiparticle systems. *J. Math. Phys.* **43**, 4273–4278 (2002).
34. Amico, L., Fazio, R., Osterloh, A. & Vedral, V. Entanglement in many-body systems. *Rev. Mod. Phys.* **80**, 517–576 (2008).
35. Brennen, G. K. An observable measure of entanglement for pure states of multi-qubit systems. *Quantum Inf. Comp.* **3**, 619–626 (2003).
36. Lee, P. A. & Ramakrishnan, T. V. Disordered electronic systems. *Rev. Mod. Phys.* **57**, 287–337 (1985).
37. Casati, G., Guarneri, I., Izrailev, F., Fishman, S. & Molinari, L. Scaling of the information length in 1D tight-binding models. *J. Phys. Cond. Mat.* **4**, 149–156 (1992).

38. Chuang, C., Lee, C. K., Moix, J. M., Knoester, J. & Cao, J. Quantum diffusion on molecular tubes: universal scaling of the 1D to 2D transition. *Phys. Rev. Lett.* **116**, 196803 (2016).
39. Varga, I. & Pipek, J. Information length and localization in one dimension. *J. Phys. Cond. Mater.* **6**, L115 (1994).
40. Van Nieuwenburg, E., Baum, Y. & Refael, G. From Bloch oscillations to many-body localization in clean interacting systems. *Proc. Natl Acad. Sci. USA* **116**, 9269–9274 (2019).
41. Guo, X. Y. et al. Observation of Bloch oscillations and Wannier-Stark localization on a superconducting processor. *npj Quantum Inf.* **7**, 51 (2021).
42. Witthaut, D., Keck, F., Korsch, H. J. & Mossmann, S. Bloch oscillations in two-dimensional lattices. *N. J. Phys.* **6**, 41 (2004).
43. Yan, F. et al. The flux qubit revisited to enhance coherence and reproducibility. *Nat. Comm.* **7**, 1–9 (2016).
44. Krantz, P. et al. A quantum engineer's guide to superconducting qubits. *Appl. Phys. Rev.* **6**, 021318 (2019).
45. Arute, F. et al. Quantum supremacy using a programmable superconducting processor. *Nature* **574**, 505–510 (2019).
46. Karamlou, A. H. et al. Analyzing the performance of variational quantum factoring on a superconducting quantum processor. *npj Quantum Inf.* **7**, 156 (2021).
47. Villa, L., Thomson, S. J. & Sanchez-Palencia, L. Quench spectroscopy of a disordered quantum system. *Phys. Rev. A* **104**, L021301 (2021).
48. Sierant, P., Delande, D. & Zakrzewski, J. Thouless time analysis of anderson and many-body localization transitions. *Phys. Rev. Lett.* **124**, 186601 (2020).
49. Khemani, V., Hermele, M. & Nandkishore, R. Localization from Hilbert space shattering: from theory to physical realizations. *Phys. Rev. B* **101**, 174204 (2020).
50. Mukherjee, B., Nandy, S., Sen, A., Sen, D. & Sengupta, K. Collapse and revival of quantum many-body scars via Floquet engineering. *Phys. Rev. Lett.* **101**, 245107 (2020).
51. Goldman, N. & Dalibard, J. Periodically driven quantum systems: effective Hamiltonians and engineered gauge fields. *Phys. Rev. X* **4**, 031027 (2014).
52. D'Alessio, L. & Rigol, M. Long-time behavior of isolated periodically driven interacting lattice systems. *Phys. Rev. X* **4**, 041048 (2014).

ACKNOWLEDGEMENTS

AUTHOR CONTRIBUTIONS

A.H.K., J.B., Y.Y., C.T., and W.D.O. conceived the experiment. A.H.K. and J.B. performed the experiments. A.H.K., J.B., B.K., M.K., A.V., R.W., and S.G. developed the experiment control tools used in this work. D.K., A.M., B.N., and J.Y. fabricated the 3×3 qubit array. C.T., T.P.O., S.G., and W.D.O. provided experimental oversight and support. All authors contributed to the discussions of the results and to the development of the manuscript.

COMPETING INTERESTS

The authors declare no competing interests.

ADDITIONAL INFORMATION

Supplementary information The online version contains supplementary material available at https://doi.org/10.1038/s41534-022-00528-0.

Correspondence and requests for materials should be addressed to Amir H. Karamlou or William D. Oliver.

Reprints and permission information is available at http://www.nature.com/reprints

Publisher's note Springer Nature remains neutral with regard to jurisdictional claims in published maps and institutional affiliations.